

to appear in Astronomical Journal (Jan 1999)

## Starburst or Seyfert? Using near-infrared spectroscopy to measure the activity in composite galaxies

Tanya L. Hill

School of Physics, University of Sydney

Charlene A. Heisler

Mount Stromlo and Siding Spring Observatories

Ralph Sutherland

Australian National University Astrophysical Theory Centre and Mount Stromlo and Siding Spring Observatories

and

Richard W. Hunstead

School of Physics, University of Sydney

### ABSTRACT

We present near-infrared spectra for a sample of galaxies with ambiguous optical emission line ratios. These galaxies fall between starbursts and Seyferts in the usual optical diagnostic diagrams. We find a similar result with the near-infrared emission line ratios, which suggests that the galaxies are composite, containing both a starburst and AGN component. Furthermore, CO absorption, produced in late-type stars, is detected within the sample, although at a weaker level than is typical for starburst galaxies. We conclude that the CO feature is being diluted by a contribution from an AGN, thereby confirming the composite nature of these galaxies.

*Subject headings:* galaxies: active — galaxies: Seyfert — galaxies: starburst

## 1. Introduction

The mechanisms by which emission lines are excited in starburst and Seyfert galaxies are not fully understood. In simplistic terms, the gas in starburst galaxies is photoionised by young, hot OB stars, whereas in Seyfert galaxies, a class of Active Galactic Nuclei (AGN), the energy is believed to be derived from photoionisation of accreting material around a supermassive black hole and the ionising spectrum takes the form of a powerlaw continuum.

There is current debate, however, over the contribution of star formation to the energy dynamics of Seyfert galaxies. At one extreme is the starburst model for AGN (Terlevich *et al.* 1992), which is claimed to be able to reproduce the properties of an AGN using compact supernova remnants (SNRs) alone, eliminating the need for a black hole entirely. Furthermore, recent findings (Boyle & Terlevich 1998) have suggested that star formation plays an important role in QSOs (more luminous AGNs), due to the striking similarity between the evolution of the QSO luminosity density and galaxy star formation rate.

It is well established that there are some galaxies in which both star formation and an AGN contribute to the observed emission, and their importance for understanding galaxy energetics is only just being realised. For example the Seyfert 2 galaxy, NGC 1068, has an extended luminous star forming region located  $\approx 3$  kpc from the central AGN (Telesco & Decher 1988), which provides half of the total luminosity of NGC 1068 (Lester *et al.* 1987; Telesco *et al.* 1984). Recent observations with the MPE 3D near-infrared (NIR) imaging spectrometer have further revealed a stellar core  $\approx 50$  pc in size that provides 7% of the nuclear bolometric luminosity of NGC 1068 (Thatte *et al.* 1997). Likewise, Genzel *et al.* (1995) have uncovered a circumnuclear ring of star formation in the Seyfert 1 galaxy NGC 7469. In this case, almost two-thirds of the total luminosity of NGC 7469 arises from starburst activity. Furthermore, a compact starburst was found in Mrk 477, an extremely luminous Seyfert 2 galaxy with a hidden Seyfert 1 component. The uncovered starburst is believed to have a bolometric luminosity comparable to the Seyfert component (Heckman *et al.* 1997).

Composite galaxies, i.e., those with both a starburst and Seyfert component, have implications for evolutionary scenarios in which one type of activity may initiate the other. For example, Norman & Scoville (1988) showed theoretically that a black hole can be formed through the evolution of a massive starburst at the centre of a galaxy. In the study of NGC 7469, Genzel *et al.* (1995) interpret a blue-shifted ridge between the nucleus and star formation ring as infalling gas providing fuel for the AGN. Alternatively, an AGN could disturb the gas in a galaxy in such a way as to trigger star formation, a mechanism proposed for the radio galaxies 3C 285 (van Breugel & Dey 1993) and Minkowski's Object

(van Breugel *et al.* 1985).

We have undertaken a search of the literature for composite galaxies based on optical spectroscopy of their nuclei as outlined in Section 2. Further in Section 2, we present photoionisation modelling of the optical emission line ratios that are commonly used as diagnostics. To gain insight into the sources of ionisation present within the galaxies we begin our investigation with NIR spectroscopy. Details of the observations and data reduction are given in Section 3. The obvious advantage of the NIR is that dust extinction is a factor of 10 lower than in the optical, thereby making it possible to probe further into the central dust-obscured regions of galaxies where the activity occurs. We explore several emission and absorption features as possible NIR ionisation diagnostics in Section 4, with the help of photoionisation models. Throughout this paper, we adopt  $H_0 = 75 \text{ km s}^{-1} \text{ Mpc}^{-1}$  and  $q_0 = 0.5$ .

## 2. Sample Selection

### 2.1. Optical Emission Line Diagnostics

Starburst galaxies and narrow line AGNs both exhibit emission lines with  $\text{FWHM} < 1000 \text{ km s}^{-1}$ . Differences in the degree of ionisation are traditionally believed to be due to the hard ionising spectrum of the AGN compared with the UV radiation from stars. It is generally accepted that AGNs contain an extended partially ionised zone. The hard X-ray component of an AGN produces high energy X-ray and far-UV photons with long mean free paths that can extend beyond the ionised region to create a large zone of partially ionised gas. For starburst galaxies, on the other hand, the transition between neutral and fully ionised gas is sharp; the UV radiation is readily absorbed by neutral hydrogen, and hence the partially ionised zone is small. The result is that the forbidden lines, e.g. [O III], [N II], [S II] and [O I], which are collisionally excited and produced mostly in partially ionised zones, are stronger in Seyfert galaxies than in starbursts. On the other hand, hydrogen recombination lines are stronger in starburst galaxies due to the H II regions surrounding young hot OB stars.

Optical emission line ratios are traditionally used to determine the photoionising source in narrow emission line galaxies. Veilleux & Osterbrock (1987) found empirically that the best optical diagnostic ratios are those of  $[\text{O III}]/\text{H}\beta$  compared with  $[\text{N II}]/\text{H}\alpha$ ,  $[\text{S II}]/\text{H}\alpha$  and  $[\text{O I}]/\text{H}\alpha$ . These line ratios are sensitive to the presence of partially ionised gas and are comprised of easily observable lines spanning a relatively narrow wavelength range, thereby minimising reddening uncertainties.

The diagnostic diagrams segregate the galaxies in the manner predicted by photoionisation models which use OB stars as the ionising source for starburst galaxies and a powerlaw input spectrum for AGN (Veilleux & Osterbrock 1987). However, not all galaxies can be easily classified using the diagnostic diagrams (eg. Ashby *et al.* 1995). In addition, photoionisation may not be the only mechanism operating to produce the narrow emission line spectra. The importance of shock excitation over photoionisation has been evaluated within the optical regime by Dopita & Sutherland (1996), who show that the spectral characteristics of many Seyfert galaxies can be produced by shock excitation alone. Shocks can have both a stellar and non-stellar origin, and are believed to be associated with supernovae in starburst galaxies and radio jets in AGN. Thus, it is important to study in detail those galaxies with ambiguous optical line ratio diagnostics in an effort to understand the mechanisms involved in producing the observed emission lines. If both star formation and an AGN are powering such galaxies, these galaxies may prove to be important for understanding the relationship, if any, between the two energy sources.

## 2.2. Sample Selection Criteria

A search of the literature was undertaken for large optical spectroscopic surveys from which to select composite galaxy candidates, that is, galaxies that potentially contain both intense star formation and an AGN. We expect that such galaxies would have ambiguous optical line ratios (intermediate to the starburst and AGN classes) and therefore used the optical diagnostic diagrams to choose galaxies that (1) fell within  $\pm 0.15\text{dex}$  of the boundary line determined by Veilleux & Osterbrock (1987) separating starburst galaxies and AGN on all three diagnostic plots, or (2) fell within the domain of starburst galaxies in one diagnostic diagram and AGN in another. The sample was constrained by a redshift upper limit of  $z = 0.035$  and declinations south of  $+24^\circ$ . From the optical spectroscopic surveys of Veilleux & Osterbrock (1987), van den Brock *et al.* (1991), Ashby *et al.* (1995) and Veilleux *et al.* (1995), we identified 34 galaxies in which the nuclear spectra have ambiguous optical line diagnostics satisfying the above criteria. NIR spectroscopy has been obtained for 12 of these galaxies and for a further five galaxies that were observed for comparison, comprising one starburst and four AGNs.

## 2.3. Modelling the Optical Diagnostics

While the segregation of starbursts and Seyferts within the optical line ratio diagnostic diagrams was discovered observationally, photoionisation models (Evans & Dopita 1985),

using hot stars and a powerlaw input spectrum to model starbursts and AGN respectively, confirm the observational finding. However, in the time since these models were calculated, knowledge of atomic structure and metal abundances has improved. Therefore, we use the latest photoionisation code MAPPINGS II (see Sutherland & Dopita 1993) to examine the dependence of the optical diagnostic line ratios on metallicity (Model A), stellar temperature and hardness of the powerlaw spectrum (Model B) and hydrogen density (Model C), according to the parameters outlined in Table 1. MAPPINGS II has also been newly expanded so that it now includes modelling of NIR emission lines (see Section 4).

The stellar atmosphere models used in MAPPINGS II are from Hummer & Mihalas (1970) and the AGN models are created from a powerlaw ionising spectrum of the form  $f_\nu \sim \nu^\alpha$ . The ionisation parameter,  $U$ , is defined by  $U = (n_H \epsilon^2 l_C)^{1/3}$ , where  $n_H$  is the total number density of hydrogen atoms and ions,  $l_C$  is the number of hydrogen-ionising photons emitted per unit time from the central source, and  $\epsilon$  is the volume filling factor (unity in our models). This parameter was varied from  $\log U = -3$  to 0 for starburst models and  $\log U = -4$  to  $-1$  for AGN models. Spherical geometry and isochoric conditions were assumed throughout.

The calculations were terminated when the fraction of neutral hydrogen reached 95% for both the starburst and AGN powerlaw models, thus permitting a uniform outer boundary condition. While a starburst model could be terminated at a higher neutral fraction, the partially ionised AGN models have numerical difficulties in achieving complete neutrality, since the thermal balance becomes due solely to X-ray ionisation and electron cascade heating. At a 95% neutral fraction, the overwhelming majority of optical and NIR emission from the models has occurred, so no significant error is introduced. The AGN models may not be accurate for far infrared fine structure lines, but these are not considered in this paper.

### 2.3.1. Model Limitations

A simplifying geometric assumption has been built into the models, namely that photoionisation occurs within a single homogeneous sphere. As a result, the partially ionised region produced by the models exists as a very thin, outer shell. In reality, the interstellar medium (ISM) is not homogeneous and a thin shell of partially ionised gas will form around each density clump found within an ionisation region. This creates a larger effective emission volume for the [S II] and [O I] lines, that are formed predominantly in partially ionised regions. As the ionisation parameter ( $U$ ) is increased within the models, corresponding to stronger [O III] emission, the partially ionised region decreases more

sharply than expected. This is because a non-homogeneous medium will contain clumps of varying density, so that even as the ionisation parameter increases the total volume of partially ionised gas can remain approximately constant. This effect causes the models to slightly underestimate emission from the partially ionised region, particularly [S II] emission. It is most pronounced in starburst models, where the partially ionised region is necessarily small due to the relatively soft radiation from stellar sources, compared with the harder ionising spectrum of a powerlaw model.

Modelling of [O I] is further limited by the complexity of the [O I] emission process. The collision strengths for transitions of the neutral [O I] species are a strong function of temperature. Further, collisions by protons and neutral hydrogen atoms can make important contributions to [O I] emission, especially in partially ionised zones that occur in AGN. However, the rates for proton and neutral hydrogen collisions are not very well known, making accurate predictions difficult for [O I] in AGN (see Williams & Livio 1995 for reviews and discussions on atomic data for emission lines). In starburst models, where the [O I] is confined to a very thin layer in the outer radii, the [O I], and to a lesser extent [S II], emission is sensitive to the chosen boundary conditions.

On the other hand, the [O III]/H $\beta$  and [N II]/H $\alpha$  ratios are comparatively more reliable, from the atomic data and modelling point of view. MAPPINGS II uses a six level atomic model for O $^{++}$  and N $^{+}$ . Electron collisions alone are the primary excitation mode for the forbidden lines and the temperature dependence of the collision strengths of these ions is relatively weak and well determined. The caveat, however, is that the [N II]/H $\alpha$  ratio is difficult to measure at low spectral resolution due to the blending of the [N II] and H $\alpha$  emission lines.

### 2.3.2. Model Analysis

The results for the three different models, defined in Table 1, are shown in Figures 1 – 3, with the starburst models denoted by ‘s’ and the powerlaw models denoted by ‘p’. The observational data are taken from Veilleux & Osterbrock (1987, and papers therein) and we also include our sample of composite galaxies.

Figure 1 shows the effect of variation in metallicity. Low and intermediate metallicities are based on the abundances of the SMC and the LMC respectively (Russell & Dopita 1990). The abundances for solar metallicity are taken from Anders & Grevesse (1989) and in a further variation, the solar abundances were depleted using the IUE data of Shull (1993).

The interesting result evident from these models occurs within the diagnostic diagram of  $[\text{O III}]/\text{H}\beta$  versus  $[\text{N II}]/\text{H}\alpha$  (Figure 1a). It can be seen that when the metallicity is below solar the powerlaw models (i.e. p1 and p2) fall into the domain of starbursts. This suggests that mis-classification of narrow emission line galaxies using the diagnostic diagrams could occur for low metallicity AGN.

Figure 2 shows the effect of stellar temperature on the starburst models and the hardness of the ionising spectrum on the AGN models. The diagrams suggest that the starburst galaxies are best modelled by high temperatures (40 000 K – 45 000 K), while the AGNs require a powerlaw index  $\alpha = -1.5$  to  $-2.0$ .

Figure 3 shows the effect of varying the hydrogen density. The powerlaw model does not converge for  $n_H = 10^2 \text{ cm}^{-3}$ , and therefore is not included in the figure. As expected, starburst galaxies are best fitted by models with  $n_H = 10^3$  to  $10^4 \text{ cm}^{-3}$ , typical of the H II regions in the Orion Nebula. A change in hydrogen density has little effect on the powerlaw models.

Overall, the starburst and powerlaw models follow the segregation of the starburst and AGN data, with the composite galaxies consistently falling between the two model types.

### 3. Observations and Reductions

Echelle spectroscopy was obtained over the period 1994 – 1996 using the InfraRed Imaging Spectrograph (IRIS) at the f/36 Cassegrain focus of the 3.9 m Anglo-Australian Telescope (AAT). Two echelles were used, the IJ echelle (0.9 – 1.5  $\mu\text{m}$ ) and the HK echelle (1.46 – 2.5  $\mu\text{m}$ ), each with spectral resolution  $\lambda/\Delta\lambda \approx 400$ . A non-destructive readout method, with read noise around 40 e<sup>–</sup> rms, was used, whereby the array is sampled regularly during an integration. This method has the advantage that data acquired after the saturation level is reached are removed. The log of the observations is presented in Table 2. Flux standards of spectral classes A and G were observed at zenith distances similar to the target galaxies. Wavelength calibration was performed using comparison lamps of helium, argon and xenon.

The galaxy spectra were reduced with the STARLINK program FIGARO using subroutines written specifically for IRIS. The observations were performed in pairs, with the galaxy positioned alternately at each end of the 13''-long slit. Subtraction of these image pairs provides a good first order sky subtraction and any residual sky is removed when pairs of extracted spectra are averaged together. A flat-field image was formed by observing the dome windscreens illuminated by a tungsten lamp; a second exposure with the lamp off was

then subtracted to remove thermal radiation from the telescope and surroundings. The flat-field image was used to remove wavelength dependent pixel-to-pixel variations across the array.

Individual bad pixels were removed from the images by linear interpolation. Straightening of the echelle orders was achieved using standard star frames, while the comparison lamp spectra were used to correct for non-vertical positioning of the slit. Before using the standard stars to flux calibrate the galaxy spectra and correct for the atmosphere, hydrogen absorption lines intrinsic to the standard were removed. Each standard star spectrum was then fitted to a blackbody model with a temperature appropriate for its spectral class.

It is important that approximately the same spatial region be examined for all the galaxies, to provide consistency in the results. We chose, therefore, to produce a nuclear spectrum by extracting pixels over a window corresponding to a linear scale of  $\approx 1$  kpc at the redshift of each galaxy. For those galaxies near the redshift upper limit of the sample ( $z = 0.035$ ), a linear scale of 1 kpc corresponds to a 2 pixel extraction box. IRIS has a pixel scale of  $0.79''/\text{pixel}$  and therefore the extraction box matches the average seeing of  $1.5''$ , obtained during the observations.

The individual orders were combined into one spectrum covering the entire IJ and HK bands. This involved bringing all the orders to the same pixel scale ( $\approx 30\text{\AA}/\text{pixel}$ ). The spectra were shifted to rest wavelength using published redshifts. Spectra of the sample of composite galaxies are shown in Figure 4 and the comparison spectra of starbursts and AGN are shown in Figure 5. The emission line fluxes were measured using the IRAF routine SPLOT, which fits a gaussian to the line profiles. The relative strengths of the emission lines are given in Tables 3 and 4 with measurement errors estimated to be  $\approx 10\%$ .

The composite galaxies with both IJ and HK data were used to form a co-added spectrum, which is shown in Figure 6. The individual galaxy spectra, all of similar slopes, were first normalised within the region  $1.5 - 1.6 \mu\text{m}$  and then averaged together. The co-added spectrum clearly brings out the emission features detected within the sample.

## 4. Results and Discussion

### 4.1. Extinction Corrections

Extinction corrections in the optical were calculated following Veilleux & Osterbrock (1987), using the Whitford reddening curve parametrized by Miller & Mathews (1972) (see

Table 5). The intrinsic  $H\alpha/H\beta$  ratio is usually set at 2.85 for starburst galaxies (assuming Case B recombination) and 3.10 for AGN, reflecting enhanced  $H\alpha$  emission due to collisional excitation. For our sample, where we are unsure of the classification, we found that neither value resolved the ambiguous nature of the line ratios and chose to adopt  $H\alpha/H\beta = 2.85$  for the composite galaxies.

Extinction in the NIR can be calculated using the NIR hydrogen recombination lines of  $Pa\beta$  and  $Br\gamma$ . However, with IRIS these two lines are recorded using different echelles,  $Pa\beta$  within IJ and  $Br\gamma$  within HK. A valid comparison requires photometric conditions during observations in both wavebands. This occurred for only three galaxies, Mrk 52, ESO 602-G025 and NGC 7130 and the values derived for the extinction from the NIR lines,  $E(B-V)_{\text{NIR}}$ , are 0.0, 1.17 and 1.23, respectively. These values for  $E(B-V)_{\text{NIR}}$  are consistent with those based on the optical line ratios for the three galaxies (see Table 5) implying that the dust is found within a homogeneous foreground screen, as opposed to it being mixed with the line-emitting gas (Puxley & Brand 1994; Calzetti *et al.* 1996).

## 4.2. Emission Features

### 4.2.1. $[Fe\text{ II}]$ Emission

In the same manner as the optical forbidden lines,  $[Fe\text{ II}]\lambda\lambda 1.25, 1.64$  is produced within regions that are partially ionised, suggesting that  $[Fe\text{ II}]$ , like  $[O\text{ I}]$  for example, might be a useful indicator of AGN activity. However,  $[Fe\text{ II}]$  can also be produced via shock excitation. In fact, strong  $[Fe\text{ II}]$  emission is found within starburst galaxies, most likely a result of shock excitation by SNRs (Mouri *et al.* 1993; Forbes & Ward 1993; Vanzi & Rieke 1997), with a possible contribution from partially ionised regions created within cooling zones formed behind the shock front in SNRs (Oliva *et al.* 1989). SNRs may also contribute to the  $[Fe\text{ II}]$  emission in AGN and, in addition, shock excitation can occur through the interaction of possible jets and outflows from the AGN with the surrounding medium.

There is some indication that  $[Fe\text{ II}]$  emission may be correlated with radio emission in starbursts and AGNs (Forbes & Ward 1993). Within starbursts the correlation is readily attributed to shock excitation from SNRs. Since both starbursts and AGNs follow the same correlation it lends support to the idea that SNRs may be producing shock excitation within AGN. However, in at least some AGNs the shock excitation is more likely associated with jet interactions, as confirmed in NGC 1068 (Blietz *et al.* 1994) where the  $[Fe\text{ II}]$  emission appears to trace the radio jet.

To further complicate matters, Fe is readily depleted onto dust grains and so the

destruction of dust grains by shocks can lead to an enhancement of [Fe II] as it is released into the gas phase (Greenhouse *et al.* 1991).

#### 4.2.2. $[\text{Fe II}]/\text{Pa}\beta$ vs $[\text{O I}]/\text{H}\alpha$

The optical line ratio,  $[\text{O I}]/\text{H}\alpha$ , is established as a reliable diagnostic for segregating AGN from starbursts (Veilleux & Osterbrock 1987), while the NIR line ratio,  $[\text{Fe II}](1.25\mu\text{m})/\text{Pa}\beta$ , has also shown promise as a good diagnostic (Simpson *et al.* 1996; Alonso-Herrero *et al.* 1997) and has a similar advantage of utilising lines close in wavelength, so reddening effects are minimised.

In Figure 7 we present a plot of  $[\text{Fe II}]/\text{Pa}\beta$  versus  $[\text{O I}]/\text{H}\alpha$  for our sample of composite galaxies, along with data from the literature (Mouri *et al.* 1990, 1993; Simpson *et al.* 1996) and photoionisation model predictions from MAPPINGS II. All the galaxies lie within the region spanned by the Orion Nebula and SNRs, which may indicate a progression from pure photoionisation to pure shock excitation (Alonso-Herrero *et al.* 1997). However, starburst galaxies have been found to lie along the mixing curve combining H II regions and SNRs, whereas Seyfert galaxies do not (Simpson *et al.* 1996). Our sample galaxies occupy the region between starbursts and Seyferts, further supporting their composite nature.

The same photoionisation models used in Section 2.3 are included in Figure 7, showing the effect of varying the metallicity, stellar temperature, powerlaw index and hydrogen density. Our results are consistent with the CLOUDY models of Alonso-Herrero *et al.* (1997), including the finding that the AGN data are best fitted by powerlaw models with low metallicity. However, Alonso-Herrero *et al.* (1997) find little difference between models with and without grains, using grain properties derived from the Orion Nebula. Our dust depletion model is based on depletion factors in the local ISM (Shull 1993), applied to a solar abundance (Anders & Grevesse 1989). We find this model to be too dusty to explain the observed  $[\text{Fe II}]/\text{Pa}\beta$  ratio, a reflection of the fact that Fe is very heavily depleted in the local ISM.

As outlined in Section 4.2.1, there is much evidence that shock excitation is the dominant mechanism for producing [Fe II] emission. Thus, it is surprising that the photoionisation models fit the data so well. Shock models of these ratios using MAPPINGS II are under development (Sutherland 1998).

Two galaxies, Mrk 52 and MCG-02-33-098, have considerably lower  $[\text{Fe II}]/\text{Pa}\beta$  ratios than the rest of the sample. In fact, Figure 7 provides strong evidence that Mrk 52 is dominated by star formation, a finding that is further supported by strong CO absorption

and  $\text{Br}\gamma$  emission (see Section 4.3.2). MCG-02-33-098 is an interacting system showing severely disturbed morphology. Of the two nuclei detected, it is the western nucleus which has a composite optical spectrum while the eastern nucleus has optical line ratios consistent with a starburst galaxy. The merger itself may be responsible for the unusual line ratios, for example by increasing shock excitation by cloud-cloud collisions. However, when we examine the optical spectrum for this galaxy (Veilleux *et al.* 1995) it appears quite noisy and the  $[\text{O I}]/\text{H}\alpha$  ratio may have been overestimated. If so, MCG-02-33-098 may move closer to the other starburst galaxies in Figure 7.

#### 4.2.3. $[\text{Fe II}]/\text{Br}\gamma$ vs $\text{H}_2/\text{Br}\gamma$

The usefulness of optical emission line diagnostic diagrams has prompted the search for similar diagrams using NIR lines. The lower dust extinction in the NIR is an advantage in probing close to the nucleus. Moorwood and Oliva (1988) proposed  $[\text{Fe II}](1.644\mu\text{m})/\text{Br}\gamma$  versus  $\text{H}_2(2.122\mu\text{m})/\text{Br}\gamma$  as a possible NIR diagnostic tool for distinguishing starburst and AGN emission, not least because these are the strongest and, therefore, the most easily measured lines. Their data suggest a segregation of starburst galaxies towards the region of low  $[\text{Fe II}]/\text{Br}\gamma$  and  $\text{H}_2/\text{Br}\gamma$  which can readily be explained by the enhanced strength of  $\text{Br}\gamma$  in starburst galaxies compared with AGN (cf. Section 2.1).

For completeness we present the NIR line ratio diagram of  $[\text{Fe II}]/\text{Br}\gamma$  versus  $\text{H}_2/\text{Br}\gamma$  in Figure 8. Our sample of galaxies is plotted together with the original measurements of Moorwood & Oliva (1988), data compiled by Forbes & Ward (1993) and blue dwarf galaxies from Vanzi & Rieke (1997). The composite galaxies, like the starbursts and Seyfert 2s, span the range from blue dwarfs to Seyfert 1s. Unfortunately, there is no strong separation of starbursts and Seyfert 2s, limiting the usefulness of this diagram as a diagnostic.

#### 4.2.4. $[\text{S III}]/\text{Pa}\beta$ vs $[\text{S II}]/\text{H}\alpha$

Emission line ratios involving sulfur have been found useful for distinguishing between photoionisation and shock excitation (Diaz, Pagel & Terlevich 1985; Diaz, Pagel & Wilson 1985). If shock excitation is occurring, it is expected that the  $[\text{S III}]$  line should be weaker than  $[\text{S II}]$  since  $\text{S}^{++}$ , in shocked gas, cools predominantly via UV line emission, corresponding to higher temperatures, rather than by emission in the NIR (Dopita 1977).

In Figure 9 we present a comparison of the sulfur line ratios  $[\text{S III}]/\text{Pa}\beta$  and  $[\text{S II}]/\text{H}\alpha$ . There is a slight tendency for the  $[\text{S III}]/\text{Pa}\beta$  ratios of the composite galaxies to favour a

starburst origin as they all lie in the region of  $\log ([\text{S III}]/\text{Pa}\beta) < 1$  which is favoured by starbursts. On the other hand, the  $[\text{S II}]/\text{H}\alpha$  line ratio is used in the diagnostic diagrams of Veilleux & Osterbrock (1987) and therefore the composite galaxies have been chosen specifically so that they lie intermediate between the starbursts and AGN. SNRs are also included in Figure 9 and fall in the region of low  $[\text{S III}]$  emission, as predicted for shock excitation.

The usual photoionisation models are also shown in Figure 9. The powerlaw models are a good fit to the AGN data. However, the starburst models are a poor fit, with the  $[\text{S III}]/\text{Pa}\beta$  ratios being too high overall to fit the starburst data. As discussed above, shocks can weaken the  $[\text{S III}]/\text{Pa}\beta$  ratio, hinting that shock excitation may be an important emission mechanism within the starburst galaxies.

### 4.3. Absorption Features

#### 4.3.1. CO Indices

Production of CO occurs in the outer envelopes of late-type stars, so the CO absorption bandhead longward of  $2.3 \mu\text{m}$  appears prominently in the spectra of red giant and supergiant stars. Evolutionary modelling (Doyon *et al.* 1994) of starburst galaxies predicts a sharp increase in CO band strength after approximately  $10^7$  yr, as red supergiants appear in the stellar population. In principle, therefore, the observed CO absorption is a means for constraining the age of a starburst.

It has only been in recent years that NIR spectroscopic detections of CO absorption in galaxies have been made and there is no clear consensus regarding the best method for measuring the strength of the absorption. The earliest CO detections, from low resolution data, show a single absorption feature longwards of  $2.3 \mu\text{m}$ . The original spectroscopic CO index ( $\text{CO}_{\text{sp}}$ ) is defined as

$$\text{CO}_{\text{sp}} = -2.5 \log_{10}(\langle R_{2.36} \rangle) \quad (1)$$

where  $\langle R_{2.36} \rangle$  is the average CO depth of the rectified spectrum between  $2.31$  and  $2.40 \mu\text{m}$  (Doyon *et al.* 1994). The rectified spectrum is obtained by fitting a powerlaw ( $f_\lambda \propto \lambda^\beta$ ) to featureless regions of the continuum between  $2.00$  and  $2.29 \mu\text{m}$  and extrapolating to longer wavelengths.  $\text{CO}_{\text{sp}}$  was defined in this manner to be compatible with the photometric CO index ( $\text{CO}_{\text{ph}}$ ) measured using narrowband filters having effective wavelengths ( $\lambda_e$ ) and FWHM ( $\Delta\lambda$ ) of  $\lambda_e = 2.20$ ,  $\Delta\lambda = 0.11 \mu\text{m}$  (continuum) and  $\lambda_e = 2.36$ ,  $\Delta\lambda = 0.08 \mu\text{m}$  (CO absorption), respectively (Frogel *et al.* 1978). A conversion between  $\text{CO}_{\text{sp}}$  and  $\text{CO}_{\text{ph}}$  is given by Doyon *et al.* (1994) based on the NIR spectroscopic stellar atlas of Kleinmann & Hall

(1986).

The main problem with the calculation of  $\text{CO}_{\text{sp}}$  as outlined above, is the wavelength range of  $2.31 - 2.40 \mu\text{m}$ . Many spectra do not extend to  $2.40 \mu\text{m}$  due to the increased thermal background at longer wavelengths hampering the detection of CO or because of the limited response of many early NIR arrays. As a result, in the CO study by Ridgway *et al.* (1994),  $\text{CO}_{\text{sp}}$  was determined using the same method as Doyon *et al.* (1994) whereby the average CO depth was measured across a rectified spectrum, except in some cases a smaller wavelength region was used, namely,  $2.31 - 2.37 \mu\text{m}$ . The resolution of these early spectra is poor but comparisons indicated that the results were consistent with Doyon *et al.* (1994). In addition, Goldader *et al.* (1995) measured  $\text{CO}_{\text{sp}}$  in the same manner, but across an even smaller wavelength region,  $2.30 - 2.34 \mu\text{m}$ .

A new method for measuring CO has recently been developed, now that increased spectral resolution reveals three distinct absorption features:  $^{12}\text{CO}$  (2,0) at  $2.294 \mu\text{m}$ ,  $^{12}\text{CO}$  (3,1) at  $2.323 \mu\text{m}$  and  $^{13}\text{CO}$  (2,0) at  $2.345 \mu\text{m}$ . The new CO measurements (Oliva *et al.* 1995; Puxley *et al.* 1997) utilize the conventional equivalent width,

$$\text{EW}(\lambda) = \int_{\lambda_{\min}}^{\lambda_{\max}} (1 - f'_\lambda) \, d\lambda, \quad (2)$$

where  $f'_\lambda$  is the normalised or rectified spectrum. Two wavelength regions have been used, the narrow region covering  $2.2931 - 2.2983 \mu\text{m}$ <sup>1</sup> and the extended region covering  $2.2931 - 2.3200 \mu\text{m}$ . These regions both include the absorption line  $^{12}\text{CO}$  (2,0). To compare with the older measurements, Puxley *et al.* (1997) determined two transformation equations to convert each equivalent width measurement (i.e., taken across the narrow region or the extended region) to the original  $\text{CO}_{\text{sp}}$  given in equation 1.

To be consistent with the literature, and to benefit future studies, we have measured the CO absorption strength using both methods and various wavelength ranges. Following Puxley *et al.* (1997), the spectra were normalised by applying a powerlaw fit to the continuum ( $f_\lambda \propto \lambda^\beta$ ) tied to featureless regions of the spectrum, namely  $2.075 - 2.100 \mu\text{m}$ ,  $2.140 - 2.150 \mu\text{m}$ ,  $2.235 - 2.240 \mu\text{m}$  and  $2.280 - 2.290 \mu\text{m}$ . The values for the  $\text{CO}_{\text{sp}}$  index determined directly from equation 1 but across various wavelength regions as indicated, are given in Table 6. The equivalent width values of CO measured directly from equation 2, are given in Table 7 for both the narrow and extended wavelength regions.

It is clear from Table 6 that the  $\text{CO}_{\text{sp}}$  index is dependent on the wavelength region used. We have also tested the transformation equations derived by Puxley *et al.* (1997) to

---

<sup>1</sup>Wavelengths quoted in this paper and Puxley *et al.* (1997) are in vacuum whereas Oliva *et al.* (1995) quote the wavelengths in air.

convert from equivalent width to  $\text{CO}_{\text{sp}}$ . In Figure 10, we compare  $\text{CO}_{\text{sp}}$  (calculated), which was calculated from the equivalent width using the Puxley *et al.* (1997) transformation, with  $\text{CO}_{\text{sp}}$  (measured) that has been determined via equation 1 using the wavelength range  $2.31 - 2.40 \mu\text{m}$ . This has been done for both the narrow and extended wavelength regions. We find that the transformation equation used to convert the equivalent width across the narrow region to  $\text{CO}_{\text{sp}}$  does not work well for our sample of composite galaxies. The statistical analysis package ASURV (LaValley, Isobe & Feigelson 1992), which implements methods for univariate and bivariate problems (Feigelson & Nelson 1985; Isobe, Feigelson & Nelson 1986) showed no significant correlation between  $\text{CO}_{\text{sp}}$  (calculated) and  $\text{CO}_{\text{sp}}$  (measured) across the narrow wavelength region. On the other hand, the transformation equation for the extended wavelength region works well. The probability that a correlation is not present between  $\text{CO}_{\text{sp}}$  (calculated) and  $\text{CO}_{\text{sp}}$  (measured) for the extended region is 0.2%, and the line of best fit has a gradient of  $1.08 \pm 0.08$ .

In all, we highlight the danger in using different measurement methods and then applying transformations to bring the values to common ground. Puxley *et al.* (1997) suggest that the equivalent width method should be used in the future to evaluate the CO absorption and that the optimal wavelength range is  $2.2931 - 2.3200 \mu\text{m}$ , that is the extended range. We agree with this choice as it covers the strongest CO absorption line, yet is a large enough region for robust measurements, as shown by our analysis of  $\text{CO}_{\text{sp}}$  (calculated) and  $\text{CO}_{\text{sp}}$  (measured). The increased resolution of NIR spectra renders the earlier method of measuring  $\text{CO}_{\text{sp}}$  via equation 1 and across large wavelength regions ( $2.31 - 2.40 \mu\text{m}$ ) obsolete.

#### 4.3.2. CO Absorption and Br $\gamma$ Emission

In starburst galaxies, CO absorption and Br $\gamma$  emission are both dependent on the age of the stellar population, with CO absorption arising from older stars and Br $\gamma$  emission resulting from the ionising UV radiation produced by young hot OB stars. As expected, models show a corresponding decrease of Br $\gamma$  emission with increasing CO absorption as a starburst population ages (Doyon *et al.* 1992).

A young starburst, less than  $10^6$  yr old, within a galaxy undergoing its first burst of star formation would theoretically be expected to exhibit strong Br $\gamma$  emission and no CO absorption. This, however, is an extreme example and unlikely to be observed in practice. Studies of low-luminosity dwarf irregular galaxies have shown that most, if not all, galaxies have undergone a succession of star formation episodes (Thuan 1983; Heisler *et al.* 1997), making it unlikely that we would ever witness a galaxy without a previous generation of

stars contributing to the CO absorption. However, in such galaxies, even with an underlying older population, the young massive stars dominate the continuum light. For example, blue compact dwarf galaxies have  $\text{Br}\gamma$  equivalent widths of order 10 nm while little or no CO absorption is detected (Vanzi & Rieke 1997).

As the starburst ages and supergiants appear in the population, CO absorption increases while  $\text{Br}\gamma$  emission drops. This is the phase in which starbursts are generally observed, corresponding to ages between  $10^6$  and  $10^8$  yr, the main-sequence lifetime of OB stars. Beyond  $10^8$  yr, when all the young OB stars have evolved, the ionising flux decreases and  $\text{Br}\gamma$  emission fades, while the CO absorption remains strong. At this stage the galaxy has CO absorption characteristic of an elliptical galaxy, which can possess  $\text{CO}_{\text{sp}}$  values as high as 0.3 (Mobasher & James 1997). The strength of CO in elliptical galaxies arises due to metallicity: giant stars with high metal abundances can have CO absorption which is as strong as the more luminous supergiants found in starbursts. An old metal rich stellar population, typical of ellipticals, can therefore resemble a starburst population in CO absorption.

Our sample of composite galaxies is compared with the data of Oliva *et al.* (1995) in Figure 11, where we use the CO equivalent width measurements between the wavelengths  $2.2931 - 2.2983 \mu\text{m}$ . The life-cycle of a starburst as outlined above, can help to explain the distribution of galaxies in this figure. Blue dwarf galaxies fall well off Figure 11 to the right, with  $\text{Br}\gamma$  equivalent widths of typically 10 nm and no CO absorption. Starburst galaxies with ages between  $10^6$  to  $10^8$  yr have consistently high CO absorption and a range of  $\text{Br}\gamma$  emission. Older starbursts such as the LMC clusters with ages  $\geq 10^8$  yr, and elliptical and spiral galaxies, show no  $\text{Br}\gamma$  and strong CO absorption. Few Seyfert galaxies have been investigated for CO absorption. The two Seyfert 1 galaxies in the study of Oliva *et al.* (1995) have no detectable  $\text{Br}\gamma$  and very weak CO absorption. The Seyfert 2s in the same study have similar CO absorption to ellipticals and spirals with some  $\text{Br}\gamma$  emission with equivalent widths of order 0.1 nm. The weak  $\text{Br}\gamma$  emission in Seyfert 2s is consistent either with emission from the narrow line region or from an old starburst.

With the exception of Mrk 52, the composite galaxies in our sample show a range of  $\text{Br}\gamma$  emission but relatively low CO absorption. Mrk 52 has the strongest CO absorption and  $\text{Br}\gamma$  emission of all the composite galaxies, supporting the earlier findings (Section 4.2.2) that Mrk 52 is probably dominated by star formation. The remaining composite galaxies do not have the extremely strong  $\text{Br}\gamma$  emission of young starbursts and the weak CO absorption suggests that we are observing older generations of stars that have already passed through the episode of peak CO production. However, these are strong optical emission line galaxies and so they must contain a nuclear ionising source. If this source is not provided

by a starburst, it is reasonable to attribute it to an AGN. To complete the picture, however, an AGN will produce a strong continuum that can weaken the CO absorption. Figure 12 shows the effect of adding an AGN component, modelled by a powerlaw spectrum of index  $\beta = -1.5$ , to the spectrum of an M5 giant star from the atlas of Kleinmann & Hall (1986). An AGN component of 50% results in a drop of  $\approx 50\%$  in the CO absorption. Therefore, a combination of an AGN plus a starburst population can explain the range of  $\text{Br}\gamma$  and CO equivalent widths found for the composite galaxies and this is also consistent with the NIR and optical emission line ratios.

#### 4.3.3. CO Absorption and Continuum Shape

When combined with a starburst population, hot dust and/or an AGN dilutes the CO equivalent width by adding a strong continuum component, especially at the red end of the K-band spectrum. To examine this effect we combined an AGN component, modelled by a powerlaw of index  $\beta = -1.5$ , with the spectrum of a M5 giant star. The powerlaw and stellar spectra were first normalised to unity using the average intensity between 2.19 – 2.21  $\mu\text{m}$ , where the continuum is predominantly featureless. The spectra were then combined using a powerlaw/stellar ratio of 0%, 25%, 50% and 75%, and the results are shown in Figure 12. Similar modelling showing the dependence of the CO absorption on extinction and hot dust emission, as well as the age of the starburst and the upper mass cut-off, can be found in Schinnerer *et al.* (1997).

To determine whether hot dust and/or an AGN is a substantial component of the sample galaxies we examine the continuum shapes as measured by the index  $\beta$  against  $\text{CO}_{\text{sp}}$  in Figure 13. We include in Figure 13 hot dust models at different temperatures, following Goldader *et al.* (1997), where a percentage of hot dust is added to an M5 giant spectrum (Kleinmann & Hall 1986). The intensity of the hot dust emission  $I(\lambda)$  is modelled by  $I(\lambda) = \lambda^{-1}B(T)$ , where  $B(T)$  is the Planck function (Emerson 1988).

Four galaxies stand out in Figure 13 by having low  $\text{CO}_{\text{sp}}$  and high  $\beta$ , consistent with the hot dust models. These include one of the AGN observed by us for comparison, Mrk 1388, and three galaxies from Ridgway *et al.* (1994) which are all classified as Seyferts (Sanders *et al.* 1988). While none of the composite galaxies show such obvious indications of an AGN and/or hot dust, they do, however, show relatively low values of  $\text{CO}_{\text{sp}}$ , which from the dust models may be the result of up to 50% dust contamination.

The data values in Figure 13 have not been corrected for extinction, which only affects the continuum shape ( $\beta$ ) and not  $\text{CO}_{\text{sp}}$  (Goldader *et al.* 1997; Schinnerer *et al.* 1997).

Since NIR extinction cannot be determined directly for all the galaxies, either because the conditions were not photometric or only one of the NIR hydrogen recombination lines was observed, we estimate the NIR extinction from the optical extinction using  $A_K = 0.108A_V$  (Mathis 1990). The maximum extinction determined for the galaxies ( $A_K = 0.6$ ), is represented by the arrow in Figure 13. Applying such an extinction to all the composite galaxies would place them close to or within the region of giants and supergiants, indicating that the galaxies contain a strong stellar population that is affected by dust.

#### 4.3.4. Other Absorption Features

As well as CO absorption, seven of the sample galaxies also show Na I (2.206  $\mu\text{m}$ ) and/or Ca I (2.263  $\mu\text{m}$ ) absorption (see Table 7). These absorption features are stronger in late-type stars with lower surface temperatures, peaking around  $T_e = 3500$  K (Kleinmann & Hall 1986). Unfortunately, it is not possible to use the Na I and Ca I absorption lines to distinguish between a normal population of giants and a starburst population of supergiants. Furthermore, there are added complications due to metallicity, with the absorption increasing for higher metal abundances.

Referring back to the optical spectra from the literature, H $\beta$  absorption is identified in all the composite galaxies. H $\beta$  absorption is weak in OB stars, peaks in A stars, before dropping off again with later spectral types. Strong H $\beta$  absorption therefore generally implies a post-starburst population. An interesting result is that AGNs have been found to have a greater mean  $\text{EW}(\text{H}\beta_{\text{abs}})$  than starburst galaxies (Veilleux *et al.* 1995). A statistical comparison of the  $\text{EW}(\text{H}\beta_{\text{abs}})$  of the composite galaxies with the starbursts and AGN using ASURV, shows that the composite galaxies more closely resemble AGN. We can reject the hypothesis of the composite galaxies and the AGN being different at the 95% confidence level, whereas there appears to be no similarity between the composite and starburst samples.

## 5. Summary

We have defined a sample of galaxies likely to contain both nuclear star formation and an AGN, based on optical emission line ratios. NIR spectroscopy of the sample has revealed that one galaxy (Mrk 52) is dominated by star formation. Otherwise, the NIR emission line ratios also tend to have values intermediate between starbursts and AGN.

The photoionisation code MAPPINGS II, which models both optical and NIR emission

lines, was used to confirm the value of emission line ratios for classifying emission line galaxies. Within the diagnostic diagrams, the models agree overall with the segregation of starburst and Seyferts seen in the observational data. From an investigation of the effect of varying metallicity within the models we found that low metallicity AGN have the potential to be mis-classified by the usual optical diagnostics as they fall within the regime of the starbursts. Furthermore, the  $[\text{Fe II}]/\text{Pa}\beta$  ratio for AGNs was found to be best fitted by a powerlaw model of low metallicity.

While shock excitation is often put forward as an important mechanism for  $[\text{Fe II}]$  emission, the photoionisation models provided a good match to the  $[\text{Fe II}]$  data. However, we did find evidence for shock excitation within the galaxies was found from the sulfur line ratios.

The stellar absorption features detected in the NIR spectra suggest the presence of an AGN. In particular, when compared with typical starburst galaxies the CO absorption is weak within the sample. We deduce that the sample galaxies are composite in nature: the starburst produces the CO absorption which is then weakened by emission from dust heated to temperatures of up to 1000 K by an AGN.

Further investigations of these galaxies are in progress. As an additional test for the presence of an AGN in the composite galaxies, we have undertaken radio continuum imaging and interferometry observations, and a paper on these results is in preparation. In addition, a program for imaging the galaxies in the optical and NIR has begun, from which colour maps will be formed to deduce the spatial distribution of the dust and star formation within the galaxies.

We would like to thank Mike Dopita, Bahram Mobasher, Jeff Goldader, Peter McGregor and Stuart Lumsden for many helpful discussions and ATAC for generous allocations of observing time. We also thank the referee for several suggestions which improved this paper. TLH acknowledges the support of an Australian Postgraduate Award and RWH acknowledges funding from the Australian Research Council. This research has made use of the NASA Astrophysics Data System service and of the NASA/IPAC Extragalactic Database which is operated by the Jet Propulsion Laboratory, California Institute of Technology, under contract with the National Aeronautics and Space Administration.

## REFERENCES

Alonso-Herrero, A., Rieke, M. J., Rieke, G. H. & Ruiz, M. 1997, *ApJ*, 482, 747.

Anders, E. & Grevesse, N. 1989 *Geochimica et Cosmochimica Acta*, 53, 197.

Ashby, M. L. N., Houck, J. R. & Matthews, K. 1995, *ApJ*, 447, 545.

Blietz, M., Cameron, M., Drapatz, S., Genzel, R., Krabbe, A., van der Werf, P., Sternberg, A. and Ward, M. 1994, *ApJ*, 421, 92.

Boyle, B. J. & Terlevich, R. J. 1998, *MNRAS*, 293, L49.

Calzetti, D., Kinney, A. L. and Storchi-Bergmann, T. 1996, *ApJ*, 458, 132.

Diaz, A. I., Pagel, B. E. J., & Terlevich, E. 1985, *MNRAS*, 214, 41.

Diaz, A. I., Pagel, B. E. J., & Wilson, I. R. G. 1985, *MNRAS*, 212, 737.

Dopita, M. A. 1977, *ApJS*, 33, 437.

Dopita, M. A. & Sutherland, R. S. 1996, *ApJS*, 102, 161.

Doyon, R., Puxley, P. J., & Joseph, R. D. 1992, *ApJ*, 397, 117.

Doyon, R., Wright, G. S., & Joseph, R. D. 1994, *ApJ*, 421, 115.

Durret, F. & Tarrab, I. 1988, *A&A*, 205, 9.

Emerson, J. P. 1988, in “Formation and Evolution of Low Mass Stars”, ed. A. K. Dupree & M. T. V. T. Lago (Dordrecht: Kluwer), 21.

Evans, I. N. & Dopita, M. A. 1985, *ApJS*, 58, 125.

Feigelson, E. D. & Nelson, P. I. 1985, *ApJ*, 293, 192.

Forbes, D. A. & Ward, M. J. 1993, *ApJ*, 416, 150.

Frogel, J. A., Persson, S. E., Aaronson, M., & Matthews, K. 1978, *ApJ*, 220, 75.

Genzel, R., Weitzel, L., Tacconi-Garman, L. E., Blietz, M., Cameron, M., Krabbe, A., Lutz, D. & Sternberg, A. 1995, *ApJ*, 444, 129.

Goldader, J. D., Goldader, D. L., Joseph, R. D., Doyon, R., & Sanders, D. B. 1997, *AJ*, 113, 1569.

Goldader, J. D., Joseph, R. D., Doyon, R., & Sanders, D. B. 1995, *ApJ*, 444, 97.

Greenhouse, M. A., Woodward, C. E., Thronson, H. A., Rudy, R. J., Rossano, G. S., Erwin, P. & Puetter, R. C. 1991, *ApJ*, 383, 164.

Heckman, T. M., Gonzalez-Delgado, R., Leitherer, C., Meurer, G. R., Krolik, J., Wilson, A. S., Koratkar, A. & Kinney, A. 1997, *ApJ*, 482, 114.

Heisler, C. A., Hill, T. L., McCall, M. L., & Hunstead, R. W. 1997, *MNRAS*, 285, 374.

Hummer, D. G., & Mihalas, D. M. 1970, *MNRAS*, 147, 339.

Isobe, T., Feigelson, E. D. & Nelson, P. I. 1986, *ApJ*, 306, 490.

Kim, K. C., Sanders, D. B., Veilleux, S., Mazzarella, J. M., & Soifer, B. T. 1995, *ApJSS*, 98, 129.

Kirhakos, S. & Phillips, M. M. 1989, *PASP*, 101, 949.

Kleinmann, S. G., & Hall, D. N. B. 1986, *ApJS*, 62, 501.

LaValley, M., Isobe, T. and Feigelson, E. D. 1992, *BAAS*, 24, 839.

Lester, D. F., Joy, M., Harvey, P. M., Ellis, H. B. & Parmer, P. S. 1987, *ApJ*, 321, 755.

Mathis, J. S. 1990, *ARA&A*, 28, 37.

Miller, J. S. & Mathews, W. C. 1972, *ApJ*, 172, 593.

Mobasher, B., & James, P. A. 1996, *MNRAS*, 280, 895.

Moorwood, A. F. M., & Oliva, E. 1988, *A&A*, 203, 278.

Mouri, H., Kawara, K. & Taniguchi, Y. 1993, *ApJ* 406, 52.

Mouri, H., Nishida, M., Taniguchi, Y., & Kawara, K. 1990, *ApJ*, 360, 55.

Norman, C. & Scoville, N. 1988, *ApJ*, 332, 124.

Oliva, E., Moorwood, A. F. M & Danziger, I. J. 1989, *A&A*, 214, 307.

Oliva, E., Origlia, L., Kotilainen, J. K. & Moorwood, A. F. M. 1995, *A&A*, 301, 55.

Osterbrock, D. E., Tran, H. D., & Veilleux, S. 1992, *ApJ*, 389, 196.

Puxley, P. J. & Brand, P. W. J. L. 1994, *MNRAS*, 266, 431.

Puxley, P. J., Doyon, R., & Ward, M. J. 1997, *ApJ*, 476, 120.

Ridgway, S. E., Wynn-Williams, C. G., & Becklin, E. E. 1994, *ApJ*, 428, 609.

Russell, S. C. & Dopita, M. A. 1990, *ApJS*, 74, 93.

Sanders, D. B., Soifer, B. T., Elias, J. H., Madore, B. F., Matthews, K., Neugebauer, G., & Scoville, N. Z. 1988, *ApJ*, 325, 74.

Schinnerer, E., Eckart, A., Quirrenbach, A., Boker, T., Tacconi-Garman, L. E., Krabbe, A., & Sternberg, A. 1997, *ApJ*, 488, 174.

Shull, J. M. 1993, *Physica Scripta*, T47, 165.

Simpson, C., Forbes, D. A., Baker, A. C. & Ward, M. J. 1996, *MNRAS*, 283, 777.

Sutherland, R. S. 1998, in preparation.

Sutherland, R. S. & Dopita, M. A. 1993, *ApJS*, 88, 253.

Telesco, C. M., Becklin, E. E., Wynn-Williams, C. G. & Harper, D. A. 1984, *ApJ*, 282, 427.

Telesco, C. M. & Drecher, R. 1988, *ApJ*, 334, 573.

Terlevich, R., Tenorio-Tagle, G., Franco, J. & Melnick, J. 1992, *MNRAS*, 255, 713.

Thatte, N., Quirrenbach, A., Genzel, R., Maiolino, R., and Tecza, M. 1997, *ApJ*, 490, 238.

Thuan, T. X. 1983, *ApJ*, 268, 667.

van Breugel, W. & Dey, A. 1993, *ApJ*, 414, 563.

van Breugel, W., Filippenko, A. V., Heckman, T. and Miley, G. 1985, *ApJ*, 293, 83.

van den Broek, A. C., van Driel, W., de Jong, T., Lub, J., de Grijp, M. H. K. & Goudfrooij, P. 1991, *A&AS*, 91, 61.

Vanzi, L., & Rieke, G. H. 1997, *ApJ*, 479, 694.

Veilleux, S., Kim, D. C., Sanders, D. B., Mazzarella, J. M. & Soifer, B. T. 1995, *ApJS*, 98, 171.

Veilleux, S. & Osterbrock, D. E. 1987, *ApJS*, 63, 295.

Williams R. & Livio, M. (eds) 1995 “The Analysis of Emission Lines”, Space Telescope Science Institute Symposium Series 8, Cambridge University Press.

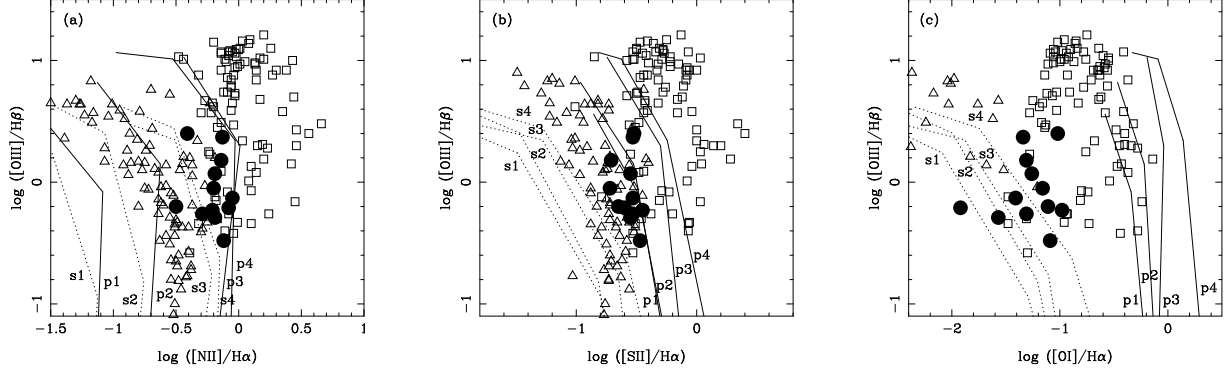


Fig. 1.— The optical diagnostic diagrams: (a)  $[\text{O III}]/\text{H}\beta$  vs  $[\text{N II}]/\text{H}\alpha$ ; (b)  $[\text{O III}]/\text{H}\beta$  vs  $[\text{S II}]/\text{H}\alpha$ ; (c)  $[\text{O III}]/\text{H}\beta$  vs  $[\text{O I}]/\text{H}\alpha$ . Symbols have the following meaning:  $\triangle$  – starbursts and  $\square$  – AGNs from the literature (Veilleux & Osterbrock 1987 and references therein);  $\bullet$  – composite galaxies from this study. The dotted lines are starburst models ( $s1, s2, s3, s4$ ) and the solid lines are powerlaw models ( $p1, p2, p3, p4$ ) from MAPPINGS II showing the effect of increasing metallicity according to Model A, defined in Table 1.

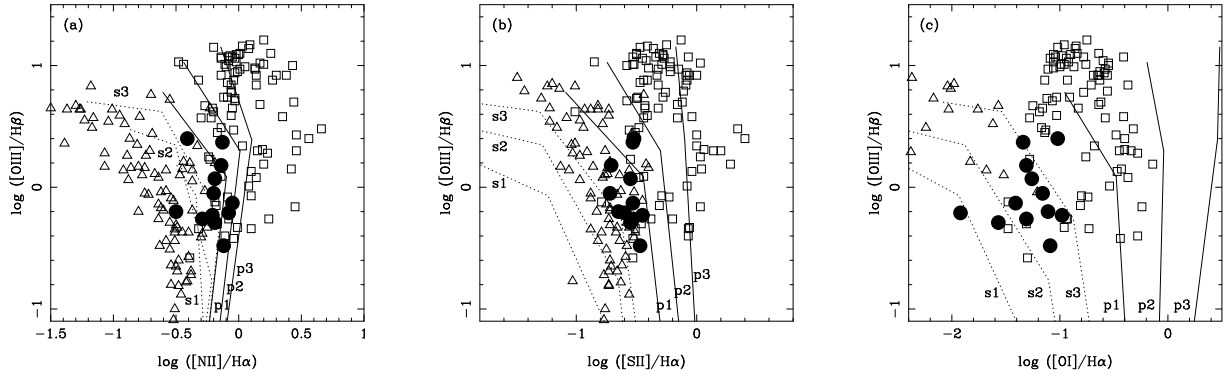


Fig. 2.— The optical diagnostic diagrams as shown in Figure 1 with the same symbol meanings. The starburst ( $s1, s2, s3$ ) and powerlaw ( $p1, p2, p3$ ) models from MAPPINGS II show the effect of increasing stellar temperature and hardness of the powerlaw spectrum respectively, according to Model B, defined in Table 1.

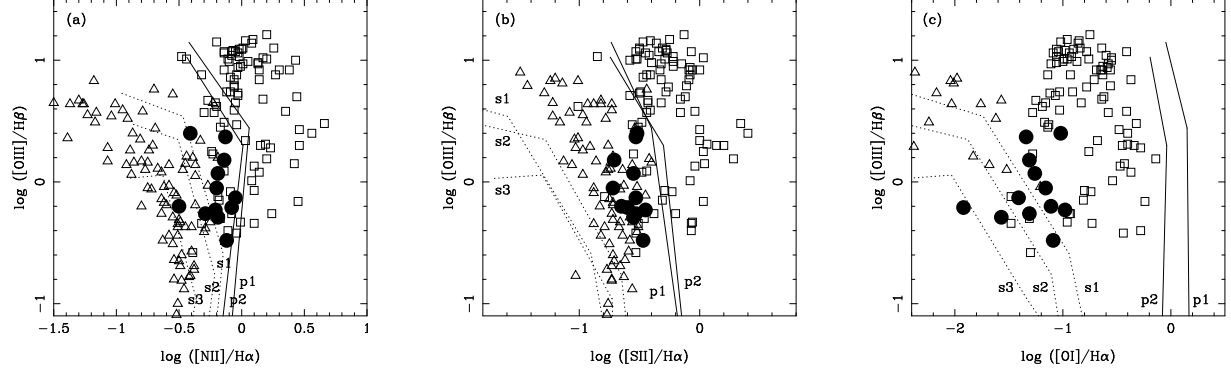


Fig. 3.— The optical diagnostic diagrams as shown in Figure 1 with the same symbol meanings. The starburst (s1, s2, s3) and the powerlaw (p1, p2) models from MAPPINGS II show the effect of decreasing hydrogen density according to Model C, defined in Table 1.

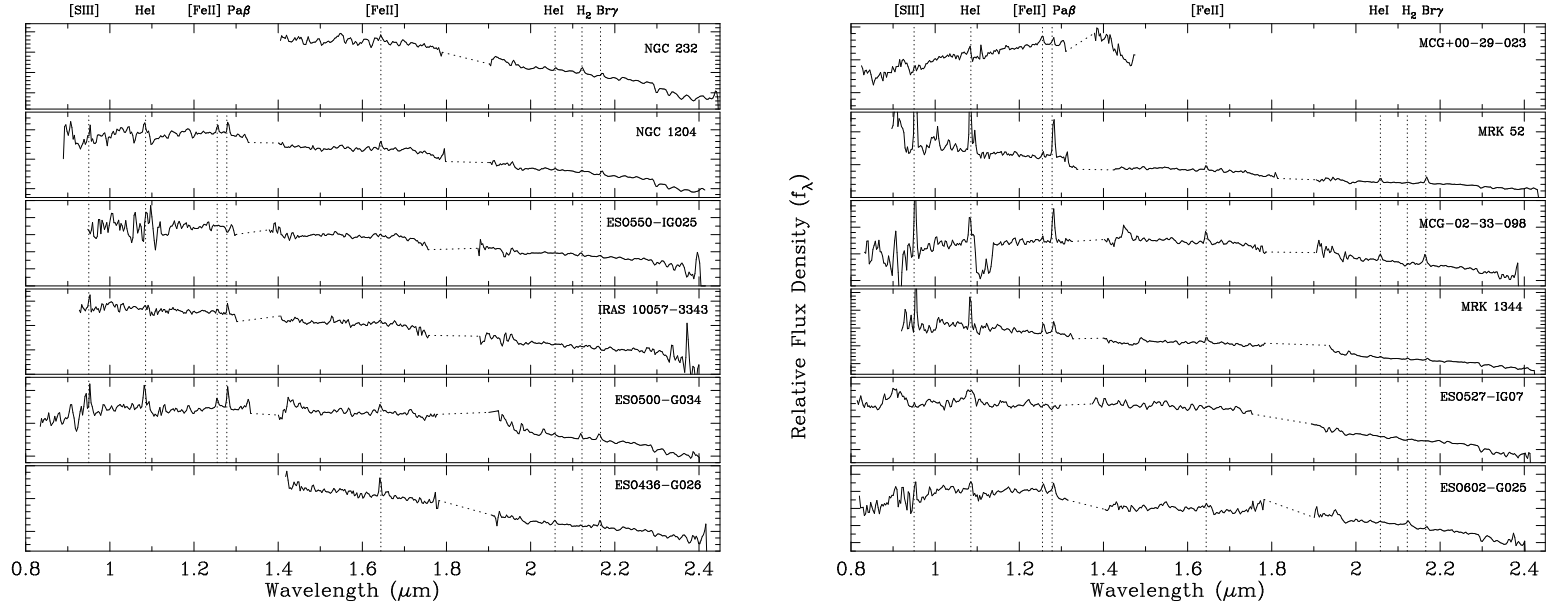


Fig. 4.— NIR spectra of the sample of composite galaxies. All spectra have been redshift corrected to the rest frame.

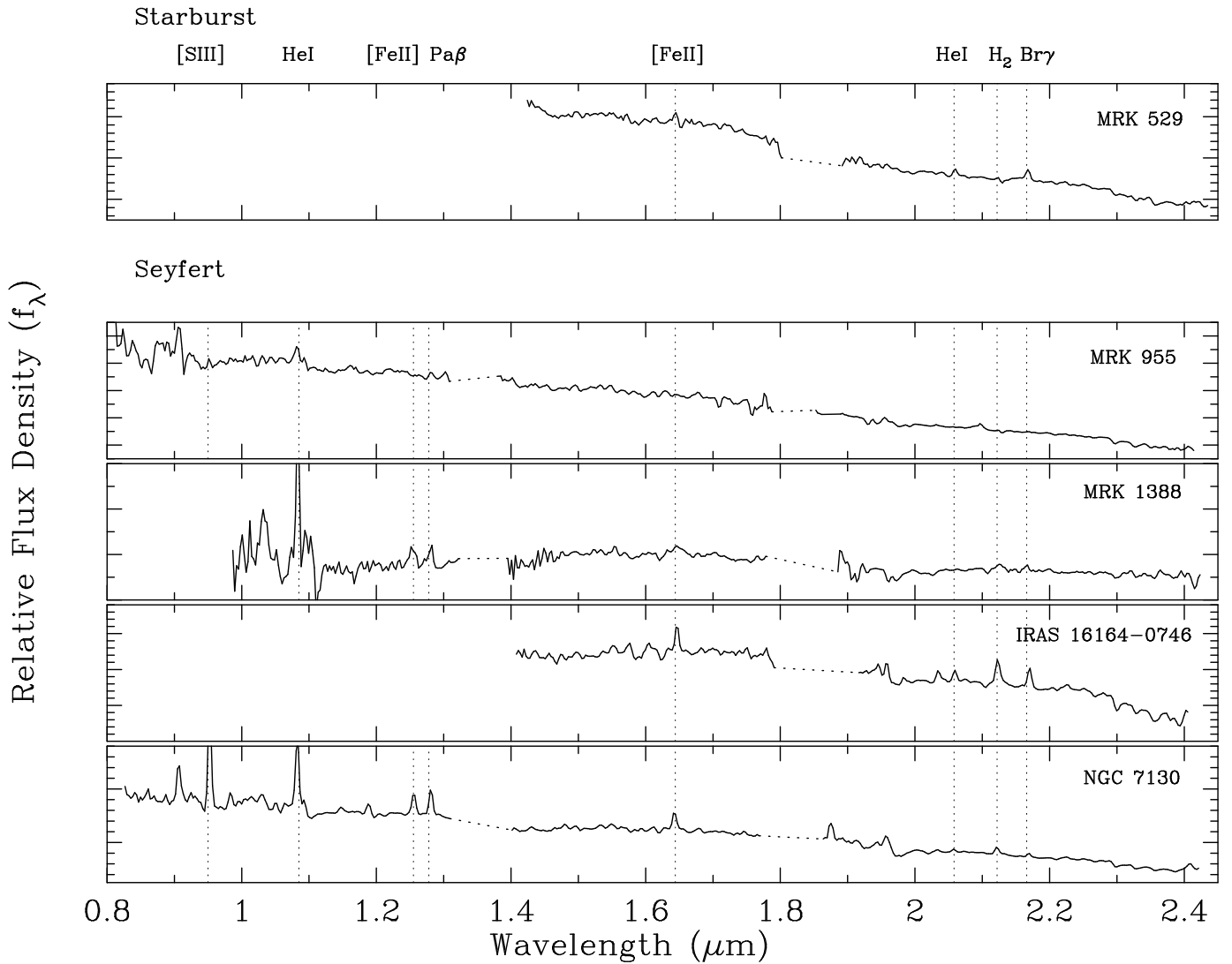


Fig. 5.— NIR spectra obtained for comparison purposes.

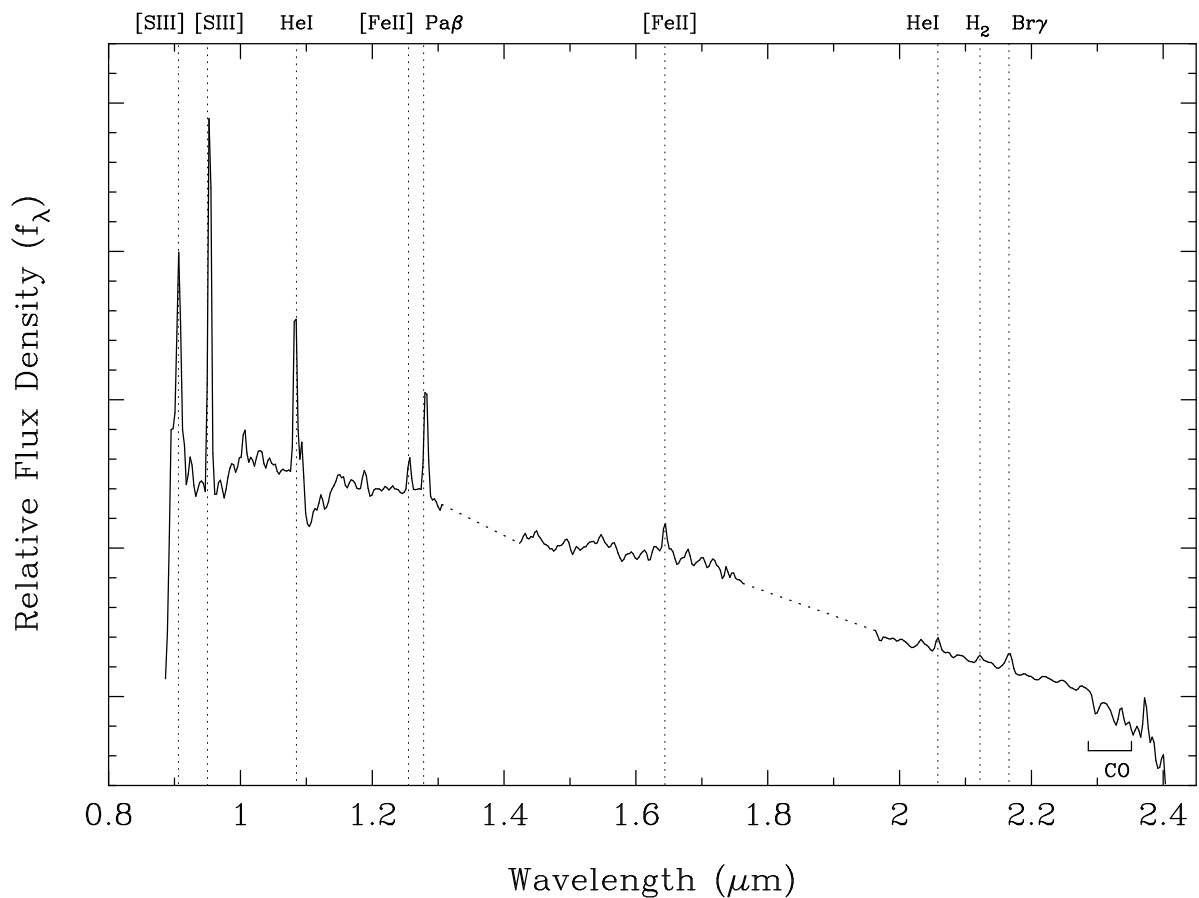


Fig. 6.— Co-added NIR spectrum formed by averaging together the spectra of the composite galaxies.

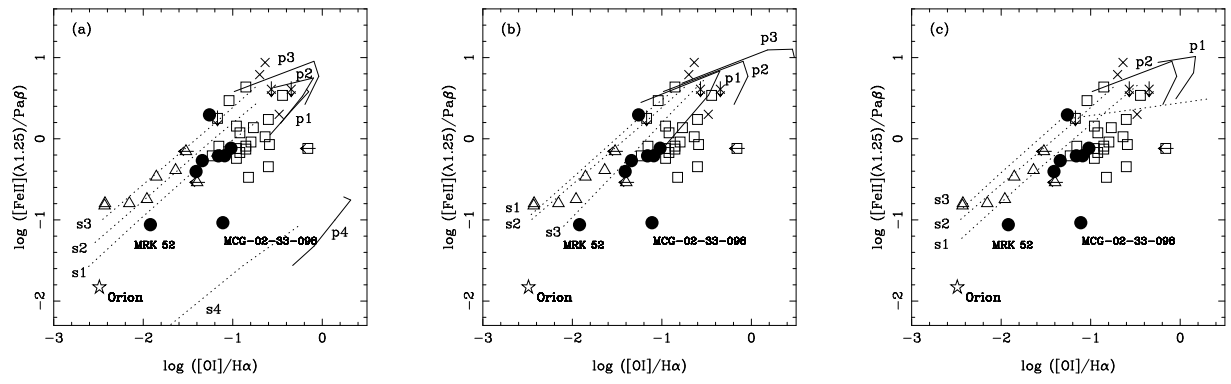


Fig. 7.— The  $[\text{Fe II}](1.25 \mu\text{m})/\text{Pa}\beta$  vs  $[\text{O I}]/\text{H}\alpha$  diagram, repeated to show the three models defined in Table 1: (a) shows the effect of varying the metal abundance (Model A); (b) shows the effect of varying the stellar temperature and powerlaw index (Model B); and (c) shows the effect of varying the hydrogen density (Model C). Symbols have the following meanings: ● – composite galaxies (optical line ratios taken from the surveys of Veilleux & Osterbrock (1987), van den Brock *et al.* (1991), Ashby *et al.* (1995) and Veilleux *et al.* (1995)); □ – AGNs (Simpson *et al.* 1996); △ – starbursts (Mouri *et al.* 1990); × – SNRs (Mouri *et al.* 1993). The Orion Nebula is also marked on the diagram (Mouri *et al.* 1993). The model labels are defined in Table 1.

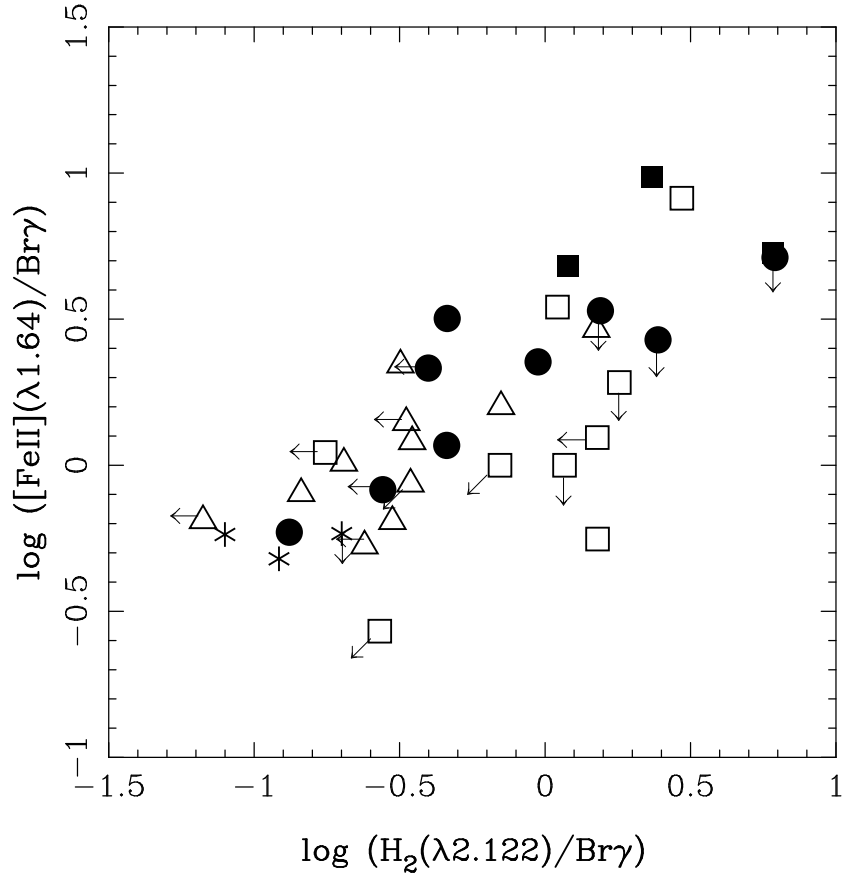


Fig. 8.— A possible NIR diagnostic diagram of  $[\text{Fe II}](1.64 \mu\text{m})/\text{Br}\gamma$  vs  $\text{H}_2(2.12 \mu\text{m})/\text{Br}\gamma$ . The symbols have the following meanings: • – composite galaxies; ■ – Seyfert 1s; □ – Seyfert 2s; △ – starbursts (Moorwood & Oliva 1988; Forbes & Ward 1993); \* – blue dwarf galaxies (Vanzi & Rieke 1997). Limits are shown with arrows.

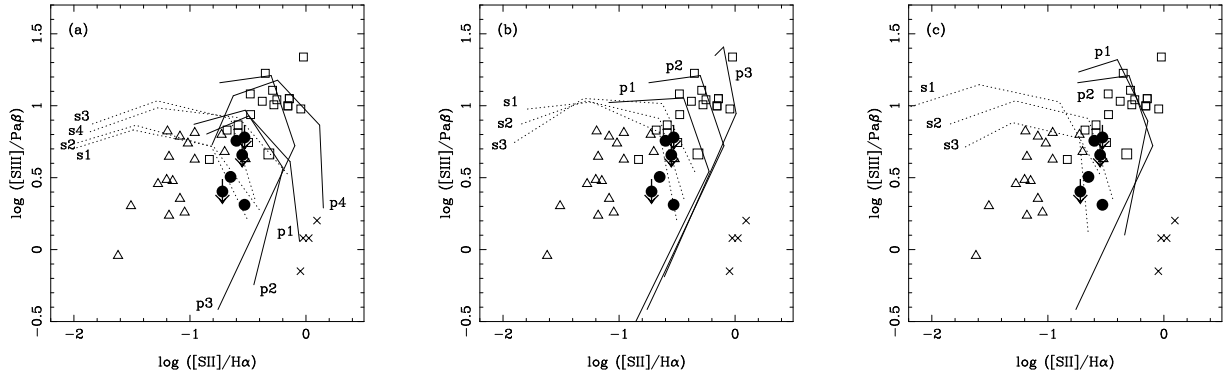


Fig. 9.— The [S III]/Pa $\beta$  vs [S II]/H $\alpha$  diagram, repeated to show the three models defined in Table 1: (a) shows the effect of varying the metal abundance (Model A); (b) shows the effect of varying the stellar temperature and powerlaw index (Model B); and (c) shows the effect of varying the hydrogen density (Model C). Symbols have the following meanings: ● – composite galaxies (optical line ratios taken from the surveys of Veilleux & Osterbrock (1987), van den Brock *et al.* (1991), Ashby *et al.* (1995) and Veilleux *et al.* (1995)); □ – AGNs; △ – starbursts; × – SNRs (Kirkhakos & Phillip 1989; Osterbrock *et al.* 1992). The model labels are defined in Table 1.

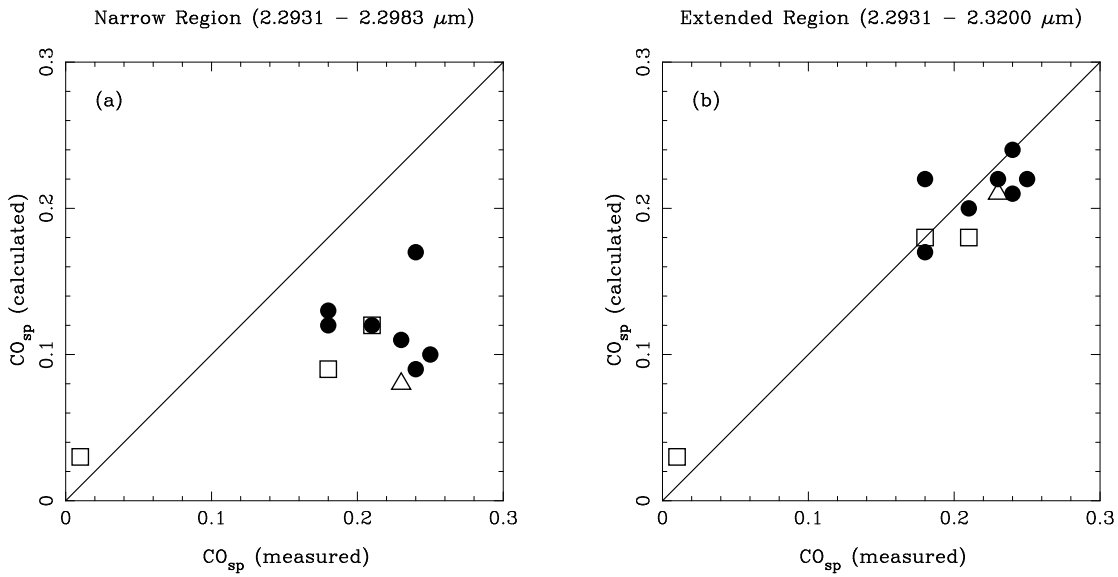


Fig. 10.—  $\text{CO}_{\text{sp}}$  (measured) was obtained directly from equation 1 across a wavelength region of  $2.31 - 2.40 \mu\text{m}$ .  $\text{CO}_{\text{sp}}$  (calculated) was obtained from the CO absorption equivalent widths and applying the transformation equations of Puxley *et al.* (1997). (a) is for the narrow region ( $2.2931 - 2.2983 \mu\text{m}$ ) and (b) is for the extended region ( $2.2931 - 2.3200 \mu\text{m}$ ). Symbols have the usual meanings: • – composites; △ – starbursts; □ – Seyfert 2s. The straight line defines equality between the two estimates.

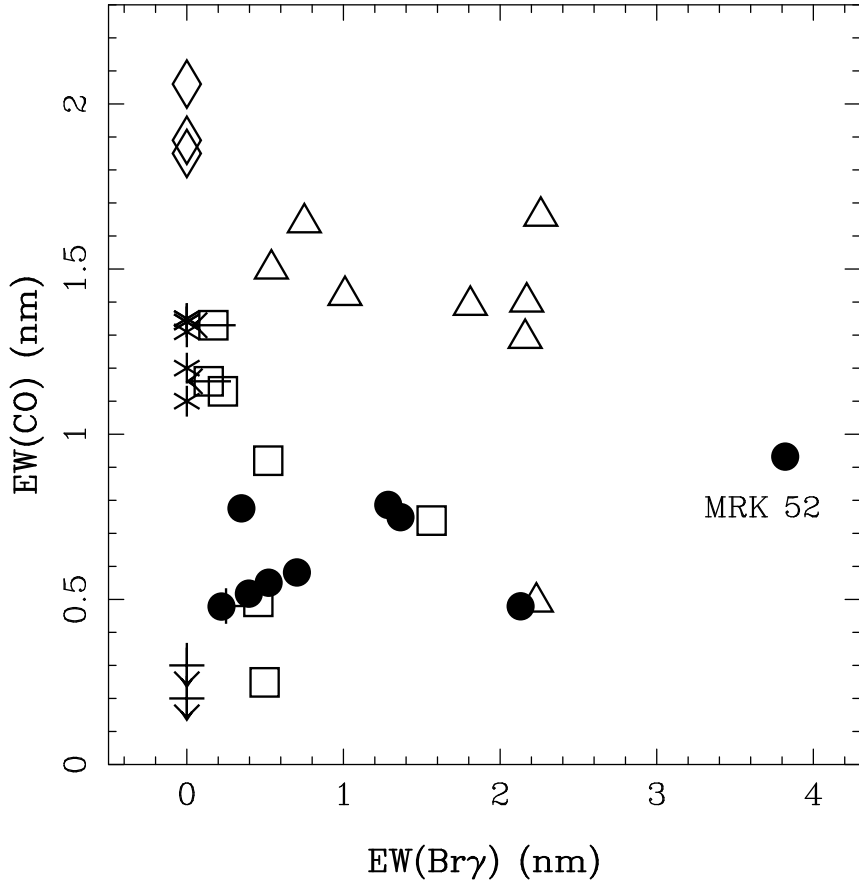


Fig. 11.— The equivalent width of CO, measured within the narrow region (2.2931 – 2.2983  $\mu\text{m}$ ), plotted against the equivalent width of Br $\gamma$ . While we believe the narrow region is not the best wavelength range to be used for measuring CO, it was necessary so that a consistent comparison could be made between the sample, shown as filled circles, and data from Oliva *et al.* (1995). The symbols have the following meaning:  $\triangle$  – starbursts;  $\square$  – Seyfert 2s;  $+$  – Seyfert 1s;  $*$  – ellipticals and spirals;  $\diamond$  – LMC clusters with ages  $<8$  Myr. Limits are shown with arrows. Note that blue dwarf galaxies fall outside the boundaries of this diagram, having  $\text{EW}(\text{Br}\gamma) \sim 10$  nm and no CO absorption (Vanzi & Rieke 1997).

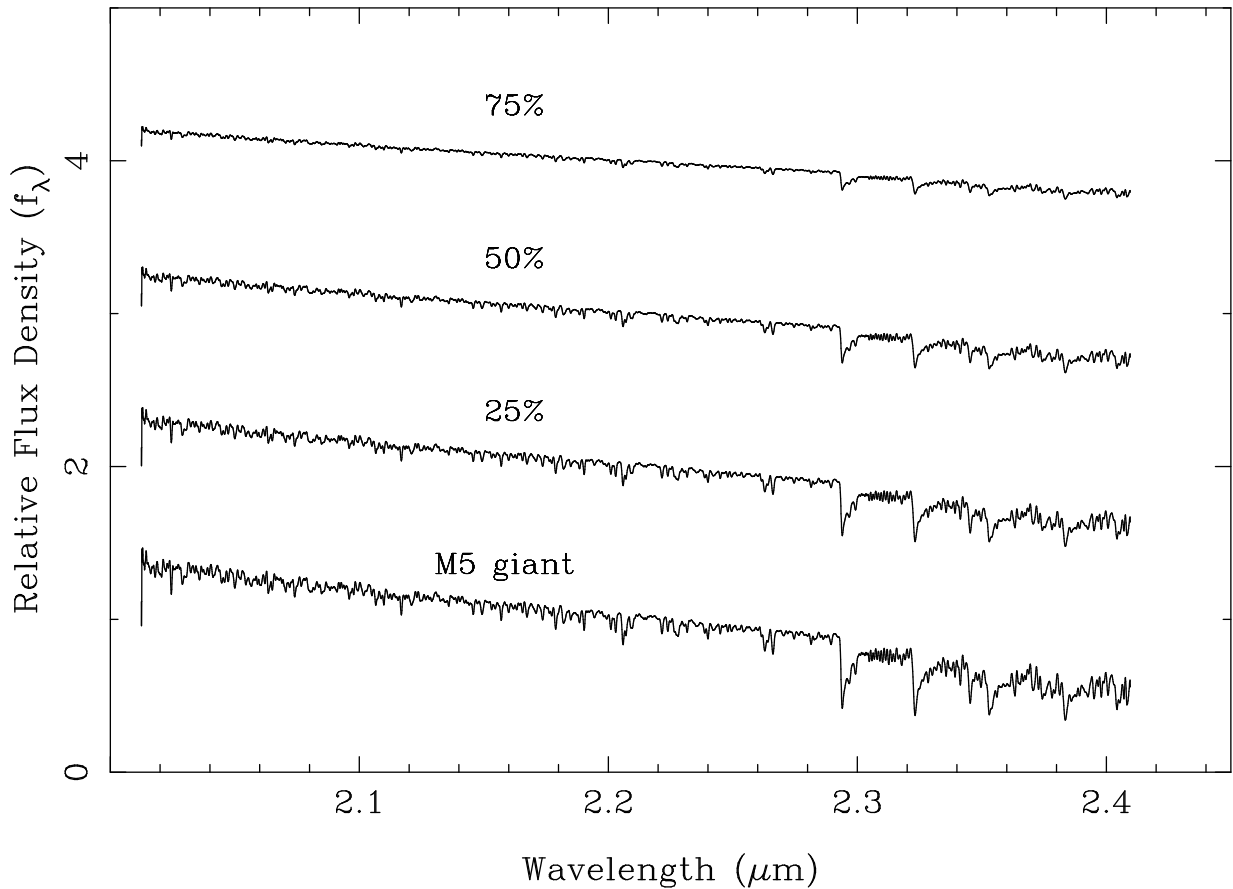


Fig. 12.— We examine the effect of adding an AGN component to the spectrum of a M5 giant star in a ratio of 25%, 50% and 75% AGN. The AGN component is modelled by a powerlaw of index  $\beta = -1.5$ . All spectra are shown to the same scale and have been shifted vertically for easy comparison.

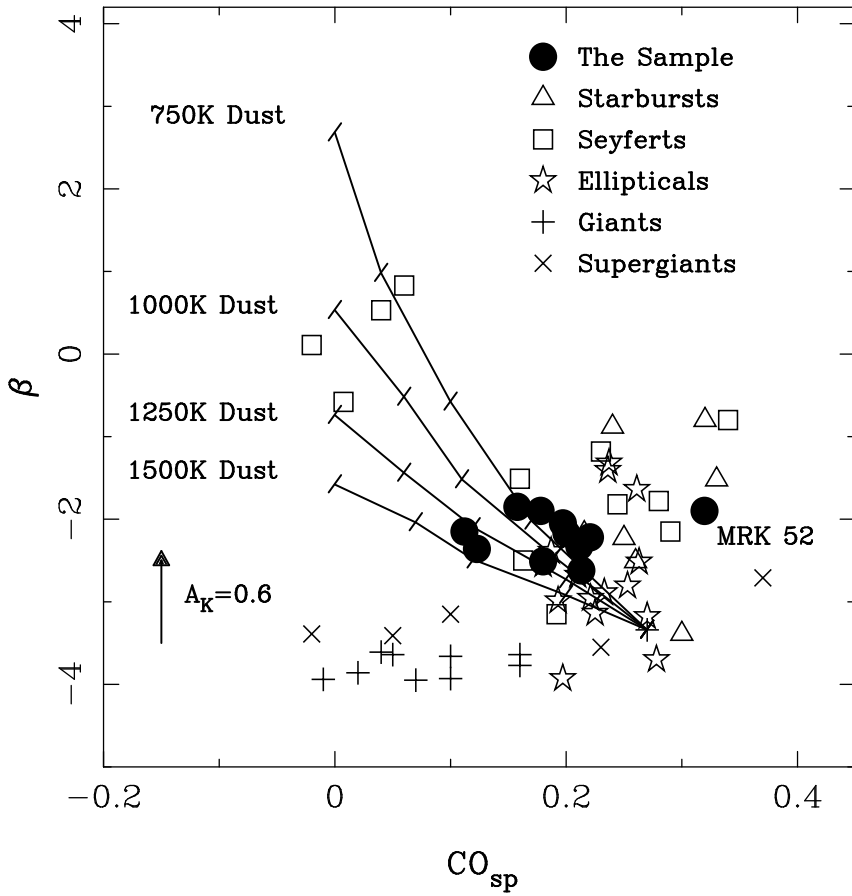


Fig. 13.— The  $\text{CO}_{\text{sp}}$  index has been measured according to Ridgway *et al.* (1994), following equation 1 and using a wavelength region of  $2.31 - 2.37 \mu\text{m}$ . While this is no longer the optimal method for measuring CO, it was necessary for consistent comparison with literature data. The  $\text{CO}_{\text{sp}}$  index is plotted against the index of the powerlaw fit to the continuum (i.e.  $f_{\lambda} \propto \lambda^{\beta}$ ). With our composite galaxy data (filled circles) we include starbursts and Seyferts (Ridgway *et al.* 1994), ellipticals (Mobasher & James 1997) and giants and supergiants from the stellar atlas of Kleinmann & Hall (1986). The curves are dust models at different temperatures, with markings representing a dust component added to a M5 giant spectrum in the ratio of 25%, 50%, 75% and 100%. The arrow shows how the addition of extinction moves a point within the diagram.

Table 1. Photoionisation model parameters

Parameter	Model A	Model B	Model C
Metallicity	s1, p1: SMC s2, p2: LMC s3, p3: solar s4, p4: depleted solar	solar	solar
Stellar Temperature (K)	40 000	s1: 38 000 s2: 40 000 s3: 45 000	40 000
Powerlaw Index ( $\alpha$ )	-1.5	p1: -2.0 p2: -1.5 p3: -1.0	-1.5
Hydrogen Density ( $\text{cm}^{-3}$ )	$10^3$	$10^3$ s2, p2: $10^3$ s3: $10^2$	s1, p1: $10^4$

Note. — The starburst photoionisation models, denoted by ‘s’, use the stellar atmosphere models of Hummer & Mihalas (1970). The powerlaw models, denoted by ‘p’, use a powerlaw ionising source of the form  $f_\nu \sim \nu^\alpha$ . The metal abundances used are based on the SMC and LMC (Russell & Dopita 1990), representing low and intermediate metallicities respectively, the solar abundances are from Anders & Grevesse (1989) and the depletion factors applied to the solar abundances were taken from Shull (1993).

Table 2. Log of AAT observations

Name	RA(2000)	Dec(2000)	z	Echelle	Date	Int. Time (s)	Obs. Cond.
NGC 232	00 42 45.9	-23 33 36	0.023	HK	15 Aug 95	4800	N
NGC 1204	03 04 40.4	-12 20 28	0.015	HK	12 Aug 95	3600	P
				IJ	13 Aug 95	1800	P
ESO 550-IG025 N	04 21 19.9	-18 48 39	0.032	HK	6 Feb 96	3600	N
				IJ	7 Feb 96	900	N
IRAS 10057-3343	10 07 59.1	-33 58 07	0.034	HK	7 Feb 96	3600	N
				IJ	7 Feb 96	5400	N
ESO 500-G034	10 24 31.4	-23 33 11	0.013	HK	5 Feb 96	3600	N
				IJ	5 Feb 96	5400	N
ESO 436-G026	10 28 42.7	-31 02 18	0.014	HK	5 Feb 96	3600	N
MCG+00-29-023	11 21 11.7	-02 59 03	0.025	IJ	7 Feb 96	5400	P
Mrk 52 (NGC 4385)	12 25 42.6	+00 34 23	0.007	HK	16 May 94	1920	P
				IJ	16 May 94	3200	P
MCG-02-33-098 W	13 02 19.9	-15 46 06	0.017	HK	6 Feb 96	600	N
				IJ	6 Feb 96	900	N
Mrk 1344 (NGC 4990)	13 09 17.2	-05 16 23	0.011	HK	17 May 94	3000	N
ESO 527-IG07	20 04 31.3	-26 25 40	0.035	HK	14 Aug 95	4800	N
				IJ	14 Aug 95	7200	N
ESO 602-G025	22 31 25.3	-19 02 05	0.025	HK	31 Oct 95	3600	P
				IJ	1 Nov 95	5400	P
Starbursts							
Mrk 529 (NGC 7532)	23 14 22.2	-02 43 39	0.010	HK	14 Aug 95	2400	P
AGN							
Mrk 955	00 37 35.8	+00 16 51	0.035	HK	13 Aug 95	3600	P
				IJ	13 Aug 95	5400	P
Mrk 1388	14 50 37.7	+22 44 04	0.021	HK	18 May 94	2400	N
				IJ	18 May 94	2400	N
IRAS 16164-0746	16 19 10.1	-07 53 57	0.021	HK	12 Aug 95	3600	P
				IJ	12 Aug 95	3600	P
NGC 7130 (IC 5135)	21 48 19.3	-34 57 03	0.016	HK	13 Aug 95	3600	P
				IJ	13 Aug 95	5400	P

Note. — Observing conditions: N – Non-photometric; P – Photometric.

Table 3. Relative intensities of emission lines in the IJ spectra

Name	[S III] $\lambda 0.90$	[S III] $\lambda 0.95$	He I $\lambda 1.085$	[Fe II] $\lambda 1.25$	Pa $\beta$ $\lambda 1.28$	Comments
NGC 232	...	...	...	...	...	no IJ spectrum
NGC 1204	...	0.81	1.59	0.62	1.0	
ESO 550-IG025 N	...	...	...	...	...	no measurable lines
IRAS 10057-3343	<4.70	<1.33	<1.20	0.40	1.0	
ESO 500-G034	1.09	0.96	1.35	0.54	1.0	
ESO 436-G026	...	...	...	...	...	no IJ spectrum
MCG+00-29-023	<2.60	1.95	1.33	1.97	1.0	
Mrk 52	1.56	4.15	1.57	0.09	1.0	
MCG-02-33-098 W	1.24	1.96	0.96	0.09	1.0	
Mrk 1344	...	3.32	2.06	0.77	1.0	
ESO 527-IG07	...	...	...	...	...	no measurable lines
ESO 602-G025	<1.48	1.06	0.96	0.62	1.0	
Starbursts						
Mrk 529	...	...	...	...	...	no IJ spectrum
AGN						
Mrk 955	...	1.10	6.58	<1.78	1.0	
Mrk 1388	...	...	5.01	1.18	1.0	
IR 16164-0746	...	...	...	...	...	no IJ spectrum
NGC 7130	1.38	3.25	2.77	0.85	1.0	

Table 4. Relative intensities of emission lines in the HK spectra

Name	H <sub>2</sub>	He I	H <sub>2</sub>	Br $\gamma$	H <sub>2</sub>	H <sub>2</sub>	Comments
	$\lambda 2.034$	$\lambda 2.058$	$\lambda 2.122$	$\lambda 2.166$	$\lambda 2.223$	$\lambda 2.248$	
NGC 232	<0.90	1.05	2.45	1.0	1.02	0.21	
NGC 1204	<0.85	<0.47	0.94	1.0	0.43	0.49	20% error in H <sub>2</sub> (2.122)
ESO 550-IG025 N	...	<0.55	1.55	1.0	...	...	
IRAS 10057-3343	...	...	...	...	...	...	no measurable lines
ESO 500-G034	0.68	0.25	0.46	1.0	0.46	0.17	
ESO 436-G026	...	0.40	<0.40	1.0	...	...	
MCG+00-29-023	...	...	...	...	...	...	no HK spectrum
Mrk 52	...	0.45	0.13	1.0	...	...	
MCG-02-33-098 W	...	0.41	<0.28	1.0	...	...	
Mrk 1344	1.21	0.52	0.46	1.0	0.53	<0.11	
ESO 527-IG07	...	...	...	...	...	...	no measurable lines
ESO 602-G025	...	<1.71	6.17	1.0	...	...	
Starbursts							
Mrk 529	...	0.25	<0.24	1.0	...	...	
AGN							
Mrk 955	...	...	...	...	...	...	no measurable lines
Mrk 1388	...	<0.35	1.80	1.0	...	...	
IRAS 16164-0746	0.20	0.28	1.51	1.0	0.50	0.33	
NGC 7130	...	0.59	2.95	1.0	1.12	0.54	

Table 5. Optical extinction data taken from the literature

Name	H $\alpha$ /H $\beta$	E(B-V)	FWHM (km s $^{-1}$ )	Ref.
NGC 232	10.5	1.32	120	1
NGC 1204	17.4	1.83	...	1
ESO 550-IG025 N	9.12	1.18	830	1
IRAS 10057-3343	17.78	1.86	300	2
ESO 500-G034	18.20	1.88	300	2
ESO 436-G026	10.72	1.34	300	2
MCG+00-29-023	12.3	1.48	660	1
Mrk 52	2.41	0.0	<260	3
MCG-02-33-098 W	12.3	1.48	1910	1
Mrk 1344	10.23	1.30	...	4
ESO 527-IG07	9.55	1.22	200	2
ESO 602-G025	10.7	1.34	800	1
Starbursts				
Mrk 529	5.50	0.67	...	4
AGN				
Mrk 955	8.13	0.98	...	4
Mrk 1388	4.57	0.39	...	4
IR 16164-0746	16.6	1.70	...	1
NGC 7130	11.22	1.30	600	2

References. — (1) Veilleux *et al.* 1995; (2) van den Broek *et al.* 1991; (3) Durrant & Tarrab 1988; (4) Veilleux & Osterbrock 1987.

Table 6. The spectroscopic CO indices and related measurements

Name	CO <sub>sp</sub> 2.31 – 2.37	CO <sub>sp</sub> 2.31 – 2.40	CO <sub>sp</sub> extended	CO <sub>sp</sub> narrow	CO <sub>sp</sub> 2.30 – 2.34	EW(Br $\gamma$ <sub>em</sub> ) nm	$\beta$
(1)	(2)	(3)	(4)	(5)	(6)	(7)	(8)
NGC 232	0.21	0.24	0.14	0.13	0.15	0.40	-2.62
NGC 1204	0.22	0.25	0.14	0.14	0.17	0.52	-2.22
ESO 550-IG025 N	0.18	...	0.08	0.18	0.11	0.35	-2.51
IRAS 10057-3343	...	...	...	...	...	...	-1.90
ESO 500-G034	0.18	0.18	0.11	0.17	0.15	1.36	-1.90
ESO 436-G026	0.16	0.18	0.14	0.17	0.17	1.29	-1.85
MCG+00-29-023	...	...	...	...	...	...	...
Mrk 52	0.21	0.24	0.15	0.22	0.18	3.82	-2.33
MCG-02-33-098 W	0.11	...	0.07	0.10	0.05	2.13	-2.15
Mrk 1344	0.20	0.23	0.14	0.15	0.16	0.70	-2.17
ESO 527-IG07	0.20	0.21	0.13	0.17	0.16	...	-2.05
ESO 602-G025	0.12	...	0.08	0.12	0.07	0.22	-2.36
Starbursts							
Mrk 529	0.22	0.23	0.13	0.12	0.17	2.23	-2.17
AGN							
Mrk 955	0.19	0.21	0.12	0.16	0.16	...	-3.15
Mrk 1388	0.01	0.01	0.02	0.06	0.0	0.50	-0.58
IRAS 16164-0746	0.24	...	0.15	0.15	0.20	1.56	-1.82
NGC 7130	0.16	0.18	0.11	0.12	0.13	0.46	-2.50

Note. — CO<sub>sp</sub> has been measured directly using equation 1 and a variety of wavelength regions.

(2): wavelength region used by Ridgway *et al.* (1994)

(3): wavelength region used by Doyon *et al.* (1994)

(4): extended region, 2.2931 – 2.3200  $\mu$ m, used by Puxley *et al.* (1997)

(5): narrow region, 2.2931 – 2.2983  $\mu$ m, used by Puxley *et al.* (1997)

(6): region used by Goldader *et al.* (1995)

(8): powerlaw index, obtained by fitting the continuum to the form  $f_\lambda \propto \lambda^\beta$

Table 7. Rest equivalent widths of absorption lines

Name	H $\beta$ $\lambda 0.4861$	Na I $\lambda 2.206$	Ca I $\lambda 2.263$	CO narrow (5)	CO extended (6)
(1)	(2)	(3)	(4)	(5)	(6)
NGC 232	0.33	1.59	2.86	0.60	3.15
NGC 1204	0.34	2.93	1.53	0.63	3.28
ESO 550-IG025 N	0.63	...	...	0.78	1.83
IRAS 10057-3343	...	...	...	...	...
ESO 500-G034	...	2.24	1.49	0.73	2.57
ESO 436-G026	...	5.62	3.88	0.77	3.15
MCG+00-29-023	0.31	...	...	...	...
Mrk 52	...	...	2.45	0.97	3.52
MCG-02-33-098 W	0.53	...	...	0.48	1.68
Mrk 1344	...	3.79	2.32	0.69	3.23
ESO 527-IG07	...	...	1.71	0.75	2.93
ESO 602-G025	0.26	...	...	0.54	1.92
Starbursts					
Mrk 529	...	...	...	0.53	3.08
AGN					
Mrk 955	...	1.94	...	0.72	2.74
Mrk 1388	...	...	1.51	0.27	0.60
IRAS 16164-0746	0.37	...	3.05	0.68	3.38
NGC 7130	...	2.36	2.37	0.56	2.68

Note. — All equivalent widths are given in nm.

(2): H $\beta$  absorption taken from Kim *et al.* (1995)

(5): narrow range, 2.2931 – 2.2983  $\mu$ m, following Puxley *et al.* (1997)

(6): extended range, 2.2931 – 2.3200  $\mu$ m, following Puxley *et al.* (1997)